

## Statistical characterization of the meteor trail distribution at the South Pole as seen by a VHF interferometric meteor radar

Elias M. Lau,<sup>1</sup> Susan K. Avery,<sup>1</sup> James P. Avery,<sup>2</sup> Diego Janches,<sup>3</sup>  
Scott E. Palo,<sup>4</sup> Robert Schafer,<sup>1</sup> and Nikolai A. Makarov<sup>5</sup>

Received 29 January 2005; revised 14 January 2006; accepted 3 March 2006; published 19 July 2006.

[1] A VHF meteor radar system was installed at the geographical South Pole in 2001. The purpose of this system is to measure the horizontal wind field in the mesosphere–lower thermosphere (MLT) region and to understand the large-scale dynamics of the Antarctic polar region. The radar operated for a few months in 2001 and with minor interruptions since that time. In this paper we will describe the meteor radar system, the data detection and collection process, and the postprocessing software that was developed to extract information from the meteor echoes collected with the interferometer that is part of the radar system. Finally, the main features of the meteor distribution will be presented and discussed. Our results show that the meteor activity peaks during the Antarctic summer. Furthermore, it occurs mostly in a small region around the ecliptic plane roughly  $\sim 20^\circ$  wide in terms of elevation angle spread.

**Citation:** Lau, E. M., S. K. Avery, J. P. Avery, D. Janches, S. E. Palo, R. Schafer, and N. A. Makarov (2006), Statistical characterization of the meteor trail distribution at the South Pole as seen by a VHF interferometric meteor radar, *Radio Sci.*, 41, RS4007, doi:10.1029/2005RS003247.

### 1. Introduction

[2] Until recently there have been few studies of the polar mesosphere–lower thermosphere (MLT,  $\sim 80$ –120 km) using ground-based techniques. This has been due in part to the harsh operating environment and geographical remoteness of the region. In 1997 the National Science Foundation (NSF) Coupling, Energetics and Dynamics of Atmospheric Regions (CEDAR) Phase III report identified the lack of measurements in the polar regions as a deficiency that must be addressed if we are to further our understanding of the globally coupled atmosphere-ionosphere system. The recommendations in this report, coupled with improved instrument reliability and increased bandwidth to observational sites

have aided in deployment of more instruments to polar regions, mostly in the Arctic. This increase in observations from the Arctic has begun to provide an improved understanding of the dynamical processes important to the Arctic region [Younger *et al.*, 2002; Mitchell *et al.*, 2002; Oznovich *et al.*, 1997]. Continued long-term observations are required if we are to understand the normal circulation patterns of the polar mesosphere and thermosphere and to separate decadal-scale solar influence from natural and anthropogenic secular changes.

[3] While the network of MLT observing stations in the Arctic has begun to mature, the Antarctic MLT observing network is still in its infancy, with only four MLT radars continuously operating in Antarctica. The goal of the meteor radar installed in 2001 (that is the focus of this paper) is to continuously run at the South Pole station and to utilize measurements of the MLT above Antarctica to answer fundamental questions pertaining to Antarctic atmospheric dynamics.

[4] Previous observations from the South Pole [Hernandez *et al.*, 1993; Portnyagin *et al.*, 1997, 1998] have elucidated the presence of a large  $s = 1$  westward propagating semidiurnal tide whose origin is unknown. This oscillation is not the typical solar forced migrating semidiurnal tide ( $s = 2$ , westward) but rather a non-migrating semidiurnal tide, which is zonally coherent and present during the summer months but disappears during the winter months. When present in the summer

<sup>1</sup>Cooperative Institute for Research in Environmental Sciences, University of Colorado, Boulder, Colorado, USA.

<sup>2</sup>Department of Electrical and Computer Engineering, University of Colorado, Boulder, Colorado, USA.

<sup>3</sup>Colorado Research Associates Division, Northwest Research Associates, Boulder, Colorado, USA.

<sup>4</sup>Department of Aerospace Engineering, University of Colorado, Boulder, Colorado, USA.

<sup>5</sup>Institute for Experimental Meteorology, Scientific Production Association TYPHOON, Obninsk, Russia.

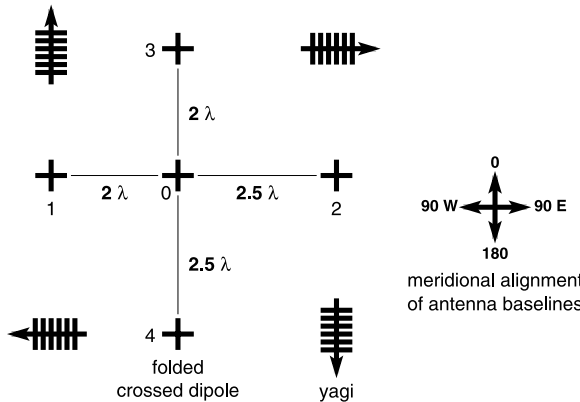


**Figure 1.** South Pole antenna layout.

this oscillation exhibits large temporal variations. The source of this nonmigrating semidiurnal tide, its seasonal structure and temporal variations are unknown. Other dynamical features such as eastward propagating planetary waves [Palo *et al.*, 1998] and Lamb waves [Hernandez *et al.*, 1992, 1996; Forbes *et al.*, 1999] have also been observed.

[5] In September 2002 the first ever Southern Hemisphere major stratospheric warming was observed [Baldwin *et al.*, 2003]. This unprecedented event split the Antarctic ozone hole into two parts. The warming was 15 K larger than the only two previous minor stratospheric warmings observed in the previous 24 years. Both temperature observations by Hernandez [2003] and wind observations by Dowdy *et al.* [2004] have indicated that the MLT dynamics were different in 2002 when compared with previous years. There is also an indication that a reversal in the MLT zonal winds occurred approximately a week prior to the warming [Dowdy *et al.*, 2004]. This could indicate a possible dynamical connection between the stratosphere and mesosphere prior to the warming. However, because of the short time series of Antarctic wind measurements continued observations are required to establish a baseline and understand the degree to which the MLT was disturbed during 2002.

[6] To improve our understanding of the Antarctic dynamics a meteor radar system was installed at the geographic South Pole in 2001 and has operated quasi-continuously since. In this paper we will describe the radar system, the detection and collection of the radar meteor echoes. We will also discuss the processing used to obtain the Doppler velocity and angle of arrival (AOA) estimates for each meteor echo. To obtain these results a precise calibration of the interferometer is needed. We will compare two different calibration techniques used for those purposes. Finally, we present and

discuss the main statistical characteristics of the meteor population observed by the radar at the South Pole.

## 2. Description of the Meteor Radar

[7] The South Pole VHF meteor radar system is a quasi all-sky system designed to measure the horizontal wind field in the MLT region. A detailed description of the radar system is given by Janches *et al.* [2004]. In this section we will only summarize some of the more important aspects of the radar.

[8] The radar system is installed approximately 1 km from the geographic South Pole. Four six-element yagi antennas horizontally mounted  $\frac{1}{2}$  wavelength above an artificial ground reflector and pointing in the directions  $0^\circ$ ,  $90^\circ\text{E}$ ,  $180^\circ$ , and  $90^\circ\text{W}$  are used for transmission and reception (Figure 1). The ground reflector creates an antenna pattern with a maximum directivity at an elevation angle of  $\sim 30^\circ$ . The yagi antennas have a theoretical full width at half power (FWHP) beam width of about  $40^\circ$ . The operating frequency of the radar is 46.3 MHz and the peak output power is 10 kW. The output is modulated by a Gaussian pulse with a width of  $36 \mu\text{s}$  and a pulse repetition frequency of 305 Hz. The yagi antennas, the radar controller, and the data acquisition system make up the Colorado Obninsk Radar (COBRA) system. The radar generally operates in a search mode in which the yagi antennas sequentially transmit a pulse one after the other. These antennas are connected through a transmit/receive (T/R) switch to a receiver. The output of the receiver is connected to a data acquisition card installed inside the computer that controls the operation of the radar system. A computer program is continuously looking for possible meteor echoes by analyzing the complex baseband output of the receiver. When the signal-to-noise ratio (SNR) increases above a predetermined threshold, the radar leaves the search mode and begins operating in an acquisition mode where the system only transmits on the antenna where a signal was detected. This allows the system to record the potential meteor echo. Once the SNR drops below 3 dB the system leaves the acquisition mode and returns to the search mode. The data is stored for further off-line processing.

[9] A second data acquisition system, Meteor Echo Detection and Collection (MEDAC) adds interferometric capabilities to this radar system. MEDAC was originally developed to be attached to VHF narrow-beam radars that measured tropospheric winds so that the dynamics of the MLT could also be studied [Avery *et al.*, 1983, 1990; Wang *et al.*, 1988; Palo and Avery, 1993, 1996; Valentic *et al.*, 1996a, 1996b, 1997a; Chang and Avery, 1997]. Over the years, MEDAC incorporated interferometric capabilities to estimate the AOA of meteor echoes and study MLT phenomena [Valentic *et al.*, 1996a; De la

[Peña *et al.*, 2005]. For the South Pole radar, MEDAC is attached to an interferometer made up of 5 folded crossed dipoles in the cross configuration introduced by Jones *et al.* [1998] (Figure 1). MEDAC is used only for reception and is synchronized with COBRA. MEDAC samples ranges between 80 and 461 km every 3 km and records five complex traces for each detected echo: one for each folded crossed-dipole antenna. The traces are analyzed later to obtain the AOA, height, and Doppler shift corresponding to each meteor echo.

[10] While data is available from both systems, in this paper we will focus on the data collected by the interferometer attached to the MEDAC system.

### 3. Data Processing

[11] After detection a time series for each event is stored for off-line processing. Each meteor echo is analyzed independently by the off-line postprocessing code. The goal of this postprocessing code is to analyze every meteor echo that was collected in the field, determine its usability (if we have too few samples of a meteor echo the estimation algorithms will not yield useful results), and estimate atmospheric parameters associated with it. For each detected meteor, we record the raw voltages coming out of the five receivers connected to the five crossed-dipole antennas. Each receiver generates a complex baseband signal, referred to as the in-phase and quadrature signal.

[12] Before the echo is subjected to any kind of analysis we smooth the collected receiver outputs. The time series were smoothed using a 5-point running average. In this paper we will often refer to the time series as the meteor trace or simply the trace. Power and phase sequences were then generated from the smoothed time series. The power sequences were then smoothed using a 5-point running average while the phase sequences were smoothed using a 9-point running average. The smoothing reduces the noise level and increases the SNR. Hence we were able to increase the percentage of meteors that are detectable by the postprocessing code and also reduce the estimation errors while keeping the signals from being completely distorted. The window sizes used for the smoothing were chosen heuristically. The effects of the smoothing are shown in Figure 2.

[13] The next step in the echo postprocessing analysis is the isolation of the echo itself since in the collected data we may have sections where only noise is present. To accomplish this we search for the peak in the power profile and we assume this is the start of the echo. The end point of the echo is chosen to be the sample where the power drops below a 6 dB threshold above the noise level measured when the meteor was detected. This echo isolation process is depicted on the right plots of Figure 2 where the signal between the dashed lines represents the

section of the collected data that is tagged as the meteor echo and is used for further postprocessing.

[14] Once the echo is isolated its Doppler frequency  $f_d$ , because of the motion of the meteor trail, is estimated using four different techniques.

[15] 1. Phase slope (PS): This method calculates the instantaneous phase from each sample of the meteor echo time series and removes any  $2\pi$  aliasing of the phase. The Doppler frequency is directly proportional to the slope of the phase, that is,  $m = 2\pi f_d$ . A linear regression is used to determine the phase slope from the phase measurements.

[16] 2. Poly-pulse pair (PPP): The phase of the complex autocorrelation function at lag  $\ell$  and sampling time  $T_s$  is  $\angle r = 2\pi f_d \ell T_s$  [Strauch *et al.*, 1978]. We compute  $\angle r$  for lags  $\ell = 0, 1, \dots, 5$ , and a least squares fit is performed to this line to estimate the Doppler frequency.

[17] 3. Maximum power spectral peak (MPSP): The frequency at which the power spectrum peaks is assumed to be the frequency due to the Doppler shift of the returned radar signal.

[18] 4. Damped sinusoid (DS): An estimator that iteratively estimates the Doppler frequency and decay rate of the meteor echo simultaneously [Tabei and Musicus, 1996].

[19] The line-of-sight or radial velocity  $v_r$  can then be calculated from the estimated Doppler frequency through the equation  $v_r = \lambda f_d / 2$ , where  $\lambda$  is the radar wavelength and  $v_r > 0$  when the meteor trail moves toward the radar.

[20] Because of system noise and different antenna sensitivities the meteor does not usually start and end on the same sample for all traces collected by the five antennas of the interferometer. For the postprocessing analysis to continue it is required that the echoes embedded in all pairs of traces (in this paper we will refer to a pair as a couple consisting of the center antenna and any of the other ones) overlap for at least five samples. If this condition is met, then the phase differences for each pair of antennas are calculated by cross correlation at lag zero. The phase differences can also be calculated as the mean of the sequence created by subtracting the unwrapped phase values for the corresponding antenna pairs. In tests (not shown here) we have conducted using simulated meteor echoes the cross correlation at lag zero proved to be the more accurate of the two approaches in the presence of noise. A third way of calculating the phase differences is calculating the cross correlation for a few different lags, perform a linear regression fit, and then calculate the fitted value at lag zero. For this approach, our simulations only show a marginal increase in accuracy while being more computationally taxing. Tests were also performed on actual meteor data and the difference in the estimates of phase differences calculated; our results show that 93% of the differences are within  $2^\circ$  and 97% are within  $3^\circ$ . Therefore we decided that

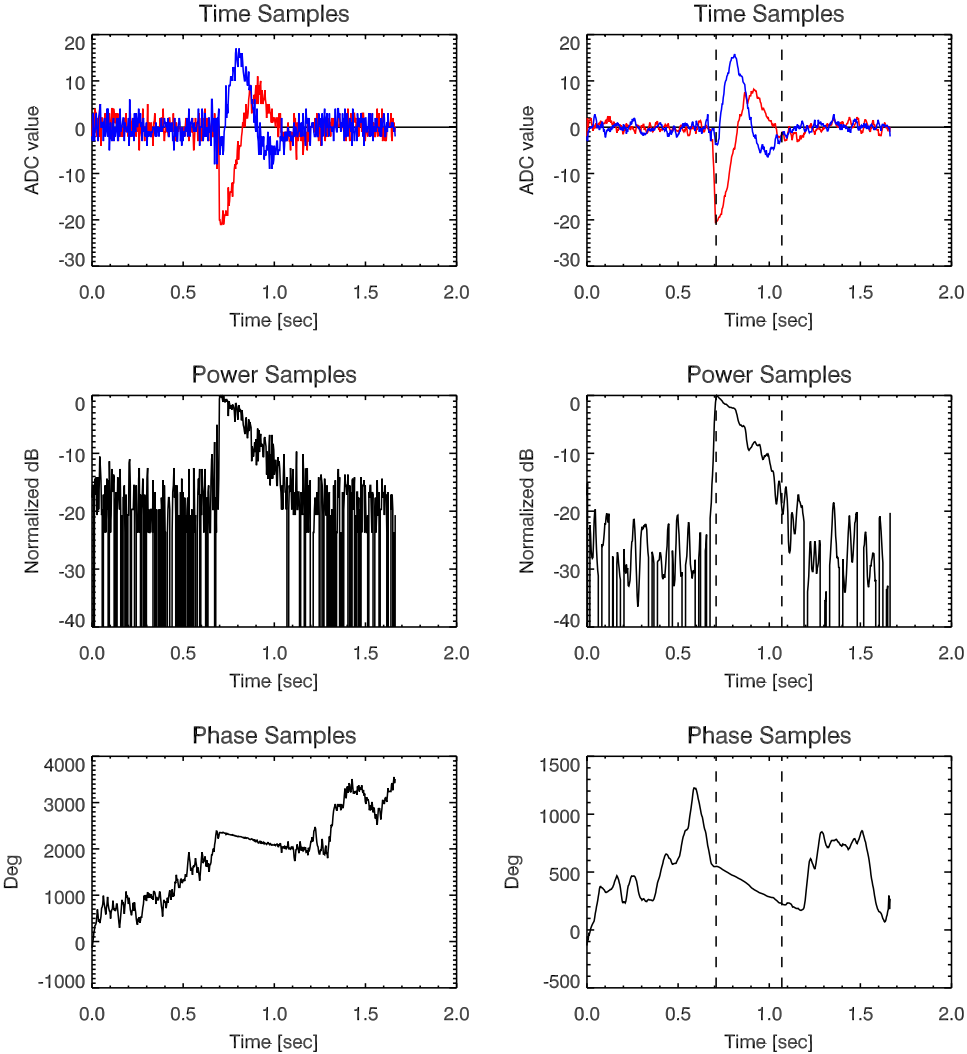


**Figure 2.** Time, power, and phase samples for a meteor echo collected by MEDAC. The left plots show the sequences before smoothing, and the right plots show the corresponding sequences after smoothing. The dashed lines on the right plots indicate the portion of the recorded data that the postprocessing code will use to estimate the meteor information.

this improvement did not outweigh the advantage of having the postprocessing code perform faster and opted for estimating the phase differences by calculating the cross correlation at lag zero. Besides, the cross correlation at lag zero method allows us to keep more of the short meteors seen by the radar. However, for sites with strong correlated noise the cross correlation at lag zero method is not recommended.

[21] Once the phase differences are estimated the AOA (the angular location of the meteor relative to the interferometer that we parameterize by an elevation angle and an azimuth—or polar—angle) of the meteor is estimated using two different algorithms. The first algo-

rithm follows the technique described by *Jones et al.* [1998]. In this algorithm an elevation angle is calculated as though the meteor is on a plane that contains three of the antennas (or baseline that includes the center antenna and antennas on either side of it) and is perpendicular to the antenna plane. Because each of the two antenna pairs along one baseline is separated by more than  $\lambda/2$ , each antenna pair yields multiple results but only one of them is the same for both pairs. The results for each baseline are then combined to estimate the three-dimensional elevation and azimuth angle of the meteor echo.

[22] The second algorithm for AOA estimation is based on the equations given by *Valentic et al.*

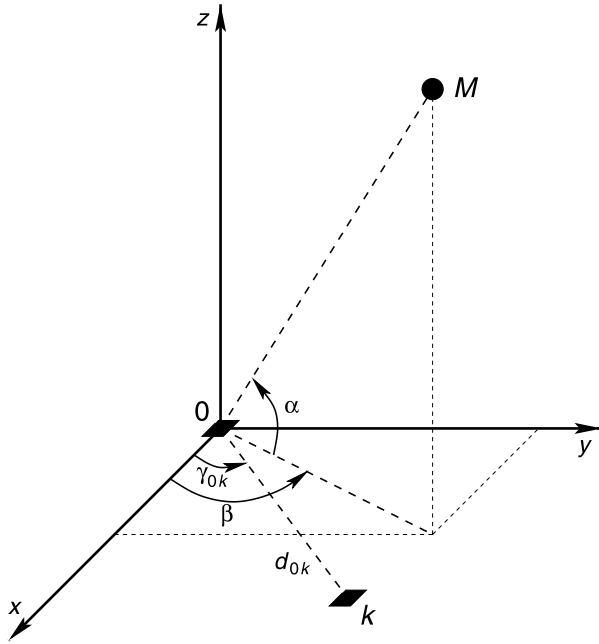


**Figure 3.** Simplified picture of the interferometer. Here 0 is the center antenna,  $k$  is one of the surrounding antennas,  $d_{0k}$  is the distance between the antennas, and  $\gamma_{0k}$  is the angle between the line where the antennas are located and the  $x$  axis. The antennas are on the  $xy$  plane.  $M$  represents the meteor,  $\alpha$  is its elevation angle, and  $\beta$  is the polar angle of its line-of-sight projection onto the  $xy$  plane.

[1997b]. We start by rewriting equations (13) through (17) from *Valentic et al.* [1997b] and adapt it for our five-antenna interferometer with a few notation changes (we explicitly include the label for the center antenna; see Figure 3):

$$\begin{bmatrix} \phi_{01} \\ \phi_{02} \\ \phi_{03} \\ \phi_{04} \end{bmatrix} = \begin{bmatrix} -\frac{2\pi}{\lambda}d_{01}\cos\gamma_{01} & -\frac{2\pi}{\lambda}d_{01}\sin\gamma_{01} \\ -\frac{2\pi}{\lambda}d_{02}\cos\gamma_{02} & -\frac{2\pi}{\lambda}d_{02}\sin\gamma_{02} \\ -\frac{2\pi}{\lambda}d_{03}\cos\gamma_{03} & -\frac{2\pi}{\lambda}d_{03}\sin\gamma_{03} \\ -\frac{2\pi}{\lambda}d_{04}\cos\gamma_{04} & -\frac{2\pi}{\lambda}d_{04}\sin\gamma_{04} \end{bmatrix} \cdot \begin{bmatrix} \cos\alpha\cos\beta \\ \cos\alpha\sin\beta \end{bmatrix} + \begin{bmatrix} \delta_{01} \\ \delta_{02} \\ \delta_{03} \\ \delta_{04} \end{bmatrix}, \quad (1)$$

where

$\phi_{0k}$  phase difference between crossed dipoles 0 and  $k$ ;

$d_{0k}, \gamma_{0k}$  interferometer geometry parameters (distances and angles; see Figure 3);  
 $\delta_{0k}$  systematic phase offset between crossed dipoles 0 and  $k$ ;  
 $\alpha$  elevation angle of the meteor  $M$ ;  
 $\beta$  polar angle of the meteor  $M$ .

[23] Equation (1) can be written as

$$\mathbf{o} = \mathbf{Sr} + \mathbf{e}, \quad (2)$$

where  $\mathbf{o}$  is a vector containing the phase differences,  $\mathbf{S}$  is a matrix whose elements are a function of the antenna pair geometries,  $\mathbf{r}$  is a vector that is a function of the AOA of the meteor, and  $\mathbf{e}$  is a vector containing the systematic phase offsets.

[24] The least squares solution of the matrix equation is

$$\mathbf{r} = \begin{bmatrix} \cos\alpha\cos\beta \\ \cos\alpha\sin\beta \end{bmatrix} = \begin{bmatrix} r_1 \\ r_2 \end{bmatrix} = (\mathbf{S}^T\mathbf{S})^{-1}\mathbf{S}^T(\mathbf{o} - \mathbf{e}). \quad (3)$$

[25] Finally, the AOA can be estimated using these equations:

$$\beta = \tan^{-1}\left(\frac{r_2}{r_1}\right), \quad \alpha = \cos^{-1}\left(\frac{r_1}{\cos\beta}\right). \quad (4)$$

[26] The phases  $\phi_{01}, \phi_{02}, \phi_{03}$ , and  $\phi_{04}$  have values that are in the range  $[-5\pi, 5\pi]$  or  $[-4\pi, 4\pi]$  depending on the distance between antennas in a pair ( $2.5\lambda$  or  $2.0\lambda$  respectively; see Figure 1). However, the phase differences  $\phi_{0k}$  ( $k = 1, \dots, 4$ ) we can calculate (using cross correlation at lag zero for instance) are in the range  $[-\pi, \pi]$ . By adding multiples of  $2\pi$  to the computed values of  $\phi_{0k}$  we can obtain

$$\begin{bmatrix} \phi_{01,j} \\ \phi_{02,j} \\ \phi_{03,j} \\ \phi_{04,j} \end{bmatrix} = \begin{bmatrix} \tilde{\phi}_{01} \\ \tilde{\phi}_{02} \\ \tilde{\phi}_{03} \\ \tilde{\phi}_{04} \end{bmatrix} + 2\pi \begin{bmatrix} n_{1,j} \\ n_{2,j} \\ n_{3,j} \\ n_{4,j} \end{bmatrix}, \quad (5)$$

where  $n$  is an integer and  $j$  indicates a particular combination of  $\{n_1, n_2, n_3, n_4\}$ . Like in the case for  $\phi_{0k}$ ,  $\phi_{0k,j}$  must have values in the range  $[-5\pi, 5\pi]$  or  $[-4\pi, 4\pi]$ . There are a finite number of combinations  $\{\phi_{01,j}, \phi_{02,j}, \phi_{03,j}, \phi_{04,j}\}$  that satisfy these conditions. Additionally, we allow the values of a combination  $\{\phi_{01,j}, \phi_{02,j}, \phi_{03,j}, \phi_{04,j}\}$  to extend  $\pi$  radians beyond the known range (e.g.,  $[-6\pi, 6\pi]$  for antennas separated by  $2.5\pi$ ) to account for imprecisions in the distances, phase estimations, etc. that can make  $\phi_{0k,j}$  fall outside the theoretical range.

[27] We can now estimate the AOA ( $\alpha_j$  and  $\beta_j$ ) using equation (4) if we substitute  $\phi_{0k,j}$  for  $\phi_{0k}$  in equation (1). We can replace the calculated values of  $\alpha_j$  and  $\beta_j$  in equation (1) and generate  $\hat{\phi}_{0k,j}$ .

[28] We define the error function in the estimated phase values as

$$E_j = \sum_{k=1}^4 \left( \hat{\phi}_{0k,j} - \phi_{0k,j} \right)^2. \quad (6)$$

[29] In theory, for a certain  $j = J$  we will have  $E_J = 0$  when  $\phi_{0k} = \phi_{0k,J}$  for  $k = 1, \dots, 4$ . This is equivalent to saying that when our guess for the AOA is the same as the actual AOA the error in the unwrapped phases goes to zero. Any other guess that does not coincide with the actual AOA will lead to a positive error, that is,  $E_{j \neq J} > 0$ . So, theoretically, we would aim for a combination of unwrapped phases that gives  $E_{j=J} = 0$ . However, in practice, for that value of  $j = J$ ,  $E_{j=J} > 0$  because of the uncertainties in the values of  $d_{0k}$ ,  $\gamma_{0k}$ ,  $\delta_{0k}$ , and  $\phi_{0k}$ . Therefore we choose the value of  $j$  that minimizes the error  $E_j$ .

[30] Applying trigonometry we utilize the estimated elevation angle and the measured echo range to calculate the vertical height of the meteor trail (see Appendix A). Since the ranges and zenith angles are large we cannot approximate the true height as the distance above a flat Earth. By taking into account the curvature of the Earth we define and calculate height as the distance in the radial direction above a spherical Earth of radius 6378.1 km.

#### 4. Testing of the Postprocessing Code

[31] We test the postprocessing code on simulated meteor echoes to gain confidence in the process and determine potential problems.

[32] We created simulated meteor echoes using the following equations

$$\left\{ \begin{array}{l} x_k(t) = Ae^{-t/\tau} \exp [j(2\pi f_d t + \phi_k)] + n(t), k = 0, 1, \dots, 4 \\ \phi_k = -\varphi_{0k} + \delta_k = -\varphi_{0k} + \delta_0 - \delta_{0k}, \delta_{0k} = \delta_0 - \delta_k \\ \varphi_{0k} = \varphi_0 - \varphi_k = -2\pi \frac{d_{0k}}{\lambda} \cos \alpha \cos(\beta - \gamma_{0k}) \\ \delta_0 = 30^\circ, \end{array} \right. \quad (7)$$

where

- $x_k(t)$  meteor signal recorded by crossed dipole  $k$ ;  $k$  follows the numbering of the crossed dipoles shown in Figure 1 and  $t$  is time;
- $A$  amplitude of the signal;
- $\tau$  decay time;
- $f_d$  line-of-sight Doppler frequency of the return signal;

$\phi_k$	phase of return signal for crossed dipole $k$ which is a function of the location of the meteor and the systematic phase offsets;
$\varphi_k$	phase associated with crossed dipole $k$ due to location of the meteor;
$\varphi_{0k}$	phase difference between crossed dipoles 0 and $k$ due to location of the simulated meteor;
$\delta_k$	systematic phase offset associated with crossed dipole $k$ ;
$\delta_{0k}$	systematic phase offset between crossed dipoles 0 and $k$ ;
$d_{0k}, \gamma_{0k}$	interferometer geometry parameters (see Figure 3);
$\alpha$	elevation angle of the simulated meteor;
$\beta$	polar angle of the simulated meteor;
$n(t)$	Gaussian complex (or circular white) noise [Stoica and Moses, 1997].

[33] To represent typical meteors, we create simulated meteor echoes on the basis of observed distributions of SNR and radial velocity during 2002. Figures 4 and 5 show histograms of SNR and radial velocity (respectively) observed by MEDAC during 2002. The SNR is calculated as the ratio (in dB) of peak power over the noise power for each meteor. The echoes detected by the MEDAC system have a SNR between  $\sim 5$  dB and  $\sim 27$  dB with a distribution peak around 13 dB. The radial velocities follow a Gaussian distribution with a mean of  $-1.6$  m/s ( $-0.5$  Hz) and a standard deviation of  $30.4$  m/s (9.4 Hz). One interesting feature of this distribution is the dip seen around 0 m/s. Reflections from stationary meteor trails come back to the receiver at exactly the same frequency as the transmitted wave. Generally, this return signal will be out of phase with the local oscillator driving the receiver. Because the two signals are mixed to produce the baseband signal, in all likelihood the output signal will experience a drop in amplitude. Therefore it is reasonable to expect a reduction in the number of echoes with no radial velocity.

[34] With the equations above and the echo statistics from Figures 4 and 5 as a guide for the typical echoes we observe at the South Pole, we generated groups of 500 meteor echoes with the following characteristics: SNRs of 10, 12, 13, 15, 16, 18, 20, or 30 dB; decay time of 0.1 s that roughly corresponds to an ablation height of 90 km at 46.3 MHz [McKinley, 1961]; Doppler frequencies of  $-10$  or  $+10$  Hz;  $d_{0k}$  and  $\gamma_{0k}$  corresponding to the crossed-dipole layout shown in Figure 1;  $\delta_{01} = -60^\circ$ ,  $\delta_{02} = -30^\circ$ ,  $\delta_{03} = -30^\circ$ , and  $\delta_{04} = -105^\circ$ ; and coming from points in the sky spaced  $10^\circ$  in azimuth and elevation angles. Elevation angles started at  $10^\circ$  and ended at  $80^\circ$  with  $10^\circ$  steps while azimuth angles started at  $0^\circ$  and ended at  $350^\circ$  with  $10^\circ$  steps.

[35] In summary, for each of the 288 points in the sky we generate 1000 different meteor echoes with the same

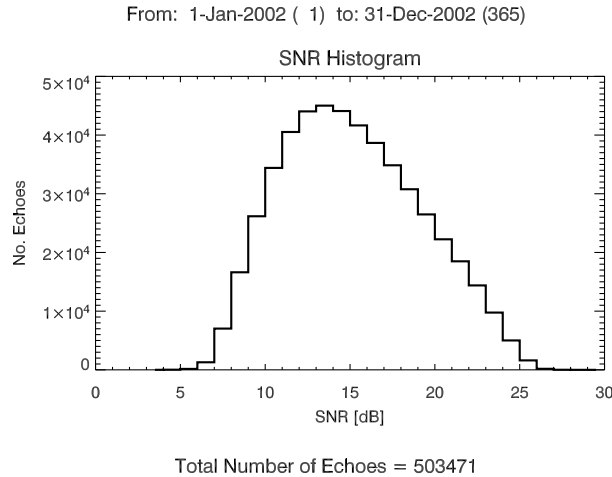


**Figure 4.** SNR histogram for all meteors detected and recorded by MEDAC in 2002. Bin size is 1 dB.

SNR and decay time; half of the 1000 simulated meteors came toward the radar while the other half moved away from it at  $|f_d| = 10$  Hz. Statistics were calculated for each of the SNR levels.

[36] In Figure 6 we show the AOA estimated errors for simulated echoes with SNR of 18 dB using the post-processing code based on the technique proposed by Jones *et al.* [1998]. The plots on the left side show the means of the errors while the plots on the right side show the standard deviations. The top plots show the absolute errors calculated as the angle in three-dimensional space between the estimated and actual AOAs. These errors are always positive and do not average out to zero. The middle plots show the errors between the estimated and actual elevation angles. Finally, the bottom plots show the errors between the estimated and actual azimuth angles. From Figure 6 it is clear that the estimation errors are larger for the lower elevation angles. A comparable plot for simulated echoes with SNR of 20 dB (not shown) exhibits similar errors to the ones presented in Jones *et al.* [1998] indicating that we have a reliable implementation of their algorithm.

[37] Figure 7 shows the same echoes when we utilize the minimum error AOA estimation algorithm (described herein). It also shows that errors are larger at low elevation angles. Estimates of the elevation angle are more prone to error at low elevation angles because  $\alpha = \cos^{-1}(r_1/\cos \beta)$  (see equation (4)) and errors in the estimation of  $(r_1/\cos \beta)$  will lead to larger errors in the estimation of  $\alpha$  when  $\alpha \approx 0$ . Estimates of the azimuth angle are less accurate at high elevation angles because azimuth angles become increasingly irrelevant and more difficult to estimate accurately (notice, for instance, that for an elevation angle of  $90^\circ$  the azimuth angle is completely unnecessary and any value is correct). How-

ever, at high elevation angles, even though the azimuth angle estimation is less accurate, the estimated AOAs are close to the actual AOAs. Comparing the statistics of the absolute errors in the top plots of Figures 6 and 7 for the different elevation angles we observe a 25–70% reduction in the mean of the errors and a 75–95% reduction in the standard deviation of the errors when using the minimum error AOA estimation algorithm. On the basis of these results we adopt this algorithm for AOA estimation of the collected data for the remainder of this paper.

[38] Figures 6 and 7 do not show the symmetry around zenith that is expected. This is very evident in Figure 6 and in a much lesser degree in Figure 7. Our analysis shows that these asymmetries are originated when the calculated phase differences between antenna pairs are imprecise. Under those circumstances the minimum error AOA estimation algorithm is better at yielding an accurate estimate of the actual AOA than the Jones *et al.* [1998] method. Furthermore, because of the noise added to the simulated signals, some angular directions are affected more than others in the estimation of the AOA contributing to the observed asymmetries.

[39] Figures 8 and 9 show results from the four Doppler velocity estimators for 12-dB and 18-dB simulated echoes respectively (28800 echoes only in each case). We observe from these two plots (and also considering simulations we have run for 13-, 15-, 16-, and 20-dB echoes not shown here) that the PS estimator does a good job of estimating the correct radial velocity at all SNR levels. The PPP method does not perform well at low SNR levels and the error distribution shows a somewhat bimodal shape. This is due to the fact that the estimator underestimates the actual radial velocity more often than it overestimates it. The MPSP estimator often performs poorly at low SNR levels but it does very well

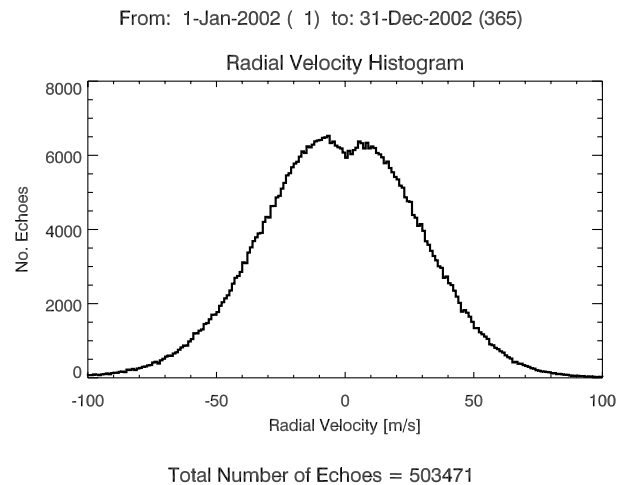


**Figure 5.** Radial velocity histogram for all meteors collected by MEDAC in 2002. Bin size is 1 m/s.

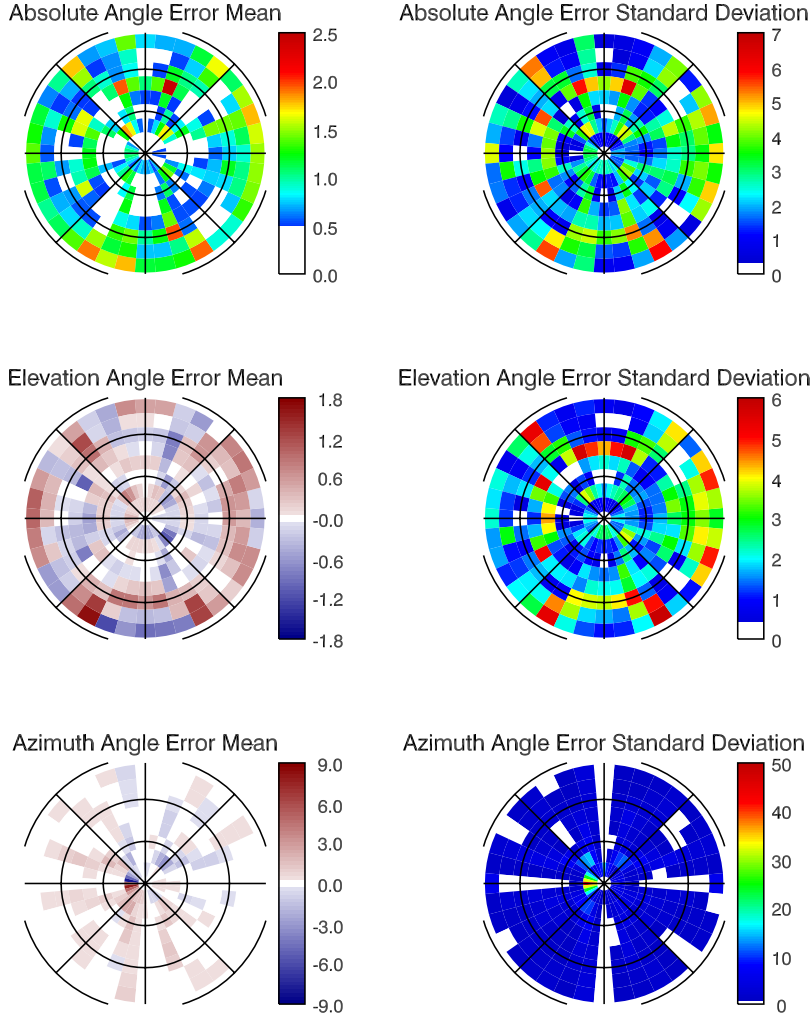


**Figure 6.** (left) Error means and (right) error standard deviations for simulated meteors with SNR = 18 dB using the algorithm based on work by Jones *et al.* [1998]. Circles represent contours of constant elevation angle from 0° (outermost) to 90° (center) in 30° steps.

once the SNR is greater than  $\sim 15$  dB. The DS estimator yields the most accurate estimates at high SNR levels but is less accurate than the PS estimator at low SNR levels.

[40] As we saw in Figure 4, we have a significant percentage of echoes that fall below SNR = 15 dB. Therefore in this paper we use the PS estimator as the algorithm to calculate the Doppler frequencies of the meteor echoes caused by the atmospheric winds.

## 5. Calibration of the MEDAC System

[41] The calibration of the MEDAC system entails the estimation of systematic phase offsets inherent to it. These phase offsets must be estimated before

postprocessing the meteor echoes because they are critical to the estimation of the AOA as shown in equation (1). The offsets may be introduced by any element of the system: crossed-dipole antennas, baluns, feed cables, receivers, and data acquisition (DAQ) cards. They are assumed to be constant and once they are estimated their values can be used to postprocess all meteors unless significant changes are made to the system (e.g., receiver tuning, cable replacement, etc.). We calibrated the system using two different techniques: the self-survey calibration technique [Valentic *et al.*, 1997b] and a phase calibration technique using a subset of the collected meteor echoes developed by Holdsworth *et al.* [2004b].

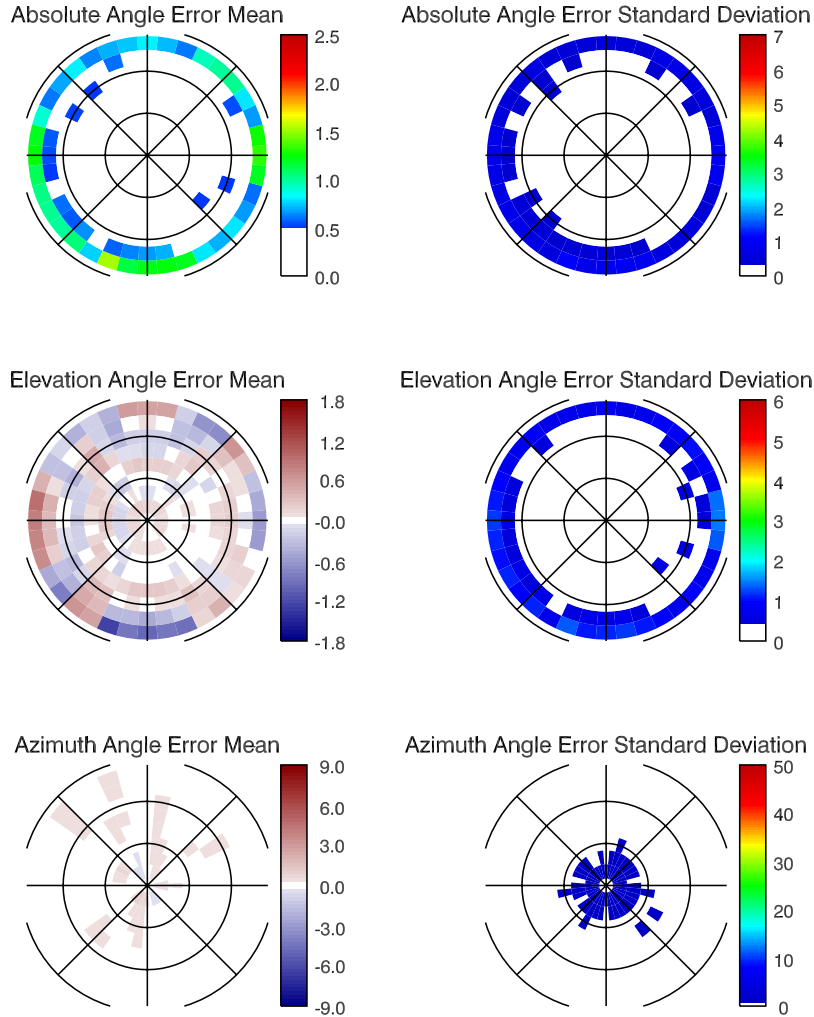


**Figure 7.** As in Figure 6 but using the iterative algorithm.

[42] For the self-survey calibration technique we marched around the antenna field with a probe antenna and a signal generator attached to it. We transmitted a continuous RF signal tens of Hz away from the radar operating frequency and had the MEDAC system collect the echoes as though they were meteors. The location of the transmit points were recorded with respect to the center antenna using a differential GPS system. Using this technique we estimated the phase offsets between the center antenna and each other antenna to be  $\delta_{01} = -62.48^\circ$ ,  $\delta_{02} = -29.93^\circ$ ,  $\delta_{03} = -32.03^\circ$ , and  $\delta_{04} = -104.08^\circ$ .

[43] For the self-survey calibration technique to be more accurate it is necessary to have transmission points as far as possible from the antennas because the algorithm assumes that the points are at infinity so that the wavefronts are planar when they reach the

antennas. Actual transmission points were within  $\sim 1$  km of the antenna array and therefore the wavefronts could have some nonnegligible curvature at the antenna array. To account for nonplanar wavefronts we calculated the phase differences for each antenna pair and added corrective phases so as to transform the results from spherical wavefronts into planar wavefronts before using the phase differences in the self-survey calibration technique. It is also desirable to have transmission points at some elevation angle to simulate operational conditions more accurately. Also, at low elevation angles we lose accuracy with the interferometry technique as shown in Figure 7 and discussed in the previous section. However, transmitting calibration signals from places far away from the radar and above the ground was not possible because of equipment and terrain limitations.

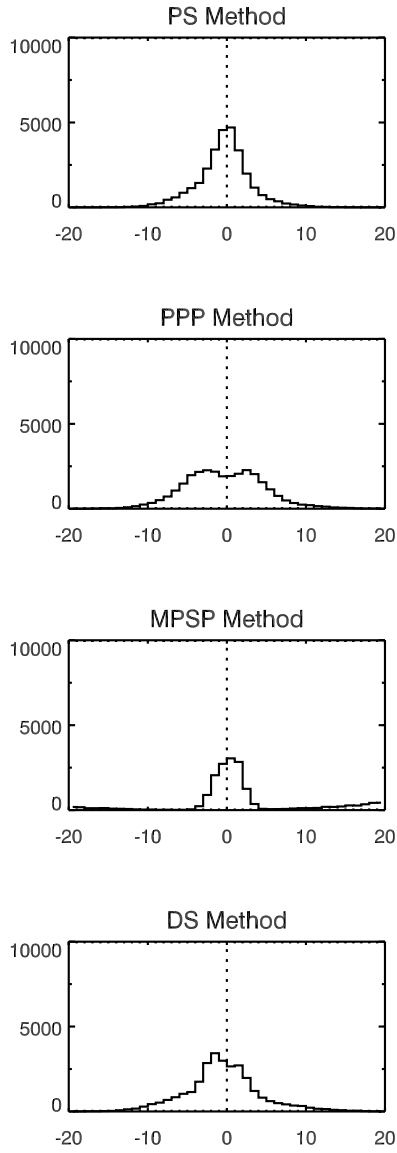


**Figure 8.** Error histograms of radial velocity for simulated meteors with SNR = 12 dB for the different radial velocity estimators.

[44] Because of the difficulties encountered in the experimental part of the self-survey calibration technique a second set of phase offsets was estimated using an independent calibration technique developed by Holdsworth *et al.* [2004b] that uses the meteor echoes collected by the radar. The phase offsets estimated by this second technique were  $\delta_{01} = -59.3^\circ$ ,  $\delta_{02} = -39.7^\circ$ ,  $\delta_{03} = -45.0^\circ$ , and  $\delta_{04} = -103.2^\circ$  using the meteor echoes collected in February 2002.

[45] We have run the meteor echoes through the postprocessing code using both sets of calibrated phase offsets. The global time, altitude and AOA distributions show negligible differences. Only when we separate echoes by their observed direction a difference in the height distributions is observed. Figure 10 shows the height distributions obtained using the phase offsets from the self-survey calibration (solid lines) as well as using the phase offsets obtained from the calibration method developed by Holdsworth *et al.* [2004b] (dotted lines). The latter shows a more consistent height distribution in

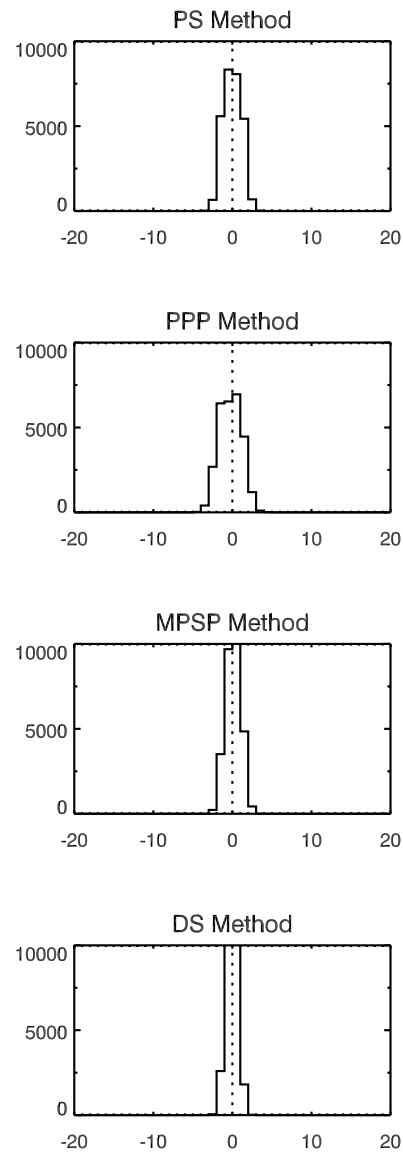


**Figure 9.** As in Figure 8 but for simulated meteors with SNR = 18 dB.

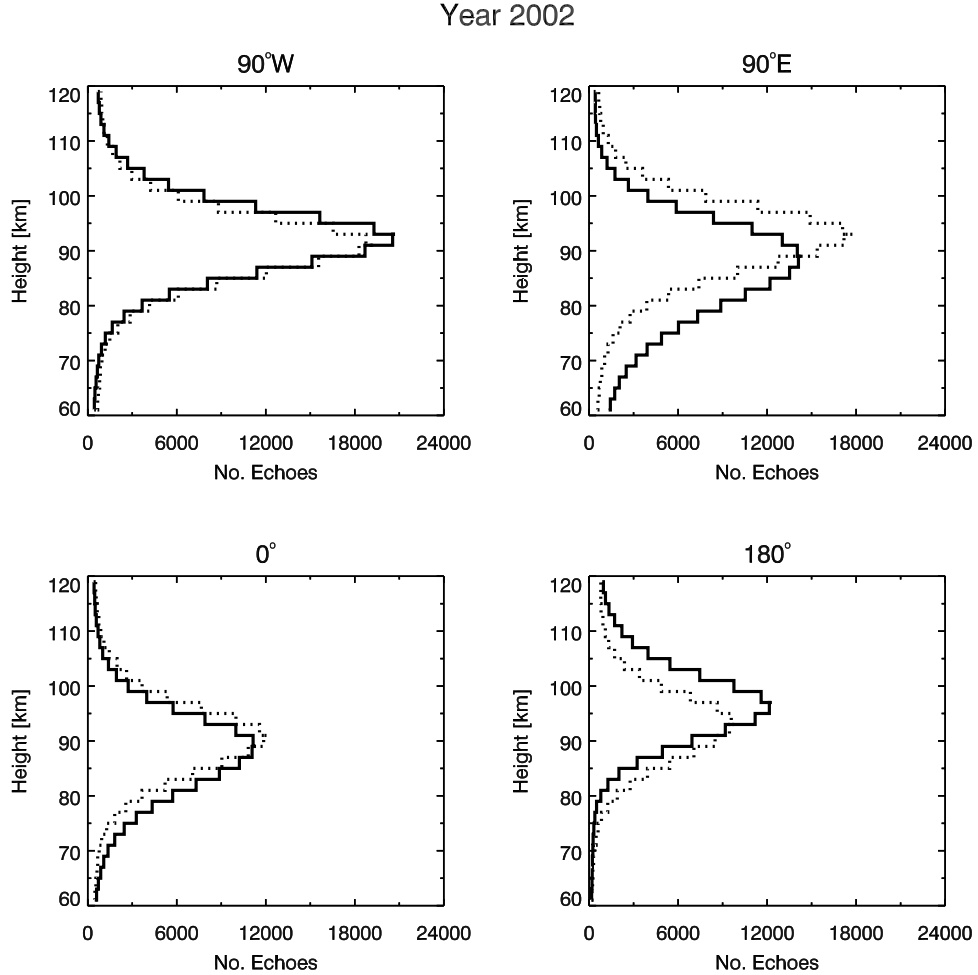


**Figure 10.** Height histograms for the different transmit antenna directions for all meteors collected by MEDAC in 2002. The solid lines are the height distributions obtained when the systematic phase offsets fed to the postprocessing code came from the self-survey calibration algorithm. The dotted lines are the height distributions obtained using the systematic phase offsets calculated by the algorithm that uses the meteor echoes themselves.

terms of peak height, width, and number of echoes along the same meridian. For this reason we will use the set of phase offsets determined by the second calibration technique in this paper when analyzing the collected meteors.

## 6. Statistical Characteristics of the Meteor Distribution

[46] In this section we present the postprocessing results of the meteor events collected during 2002 and 2003. Meteors with estimated heights below 60 km and above 120 km were removed from the final results. Between 40% and 50% of the meteor echoes collected

in the field are represented in the plots shown in this section. The majority of the meteor echoes not shown in the following plots were filtered out by the postprocessing algorithm while a smaller fraction was dismissed because their estimated altitudes did not fall in the 60–120 km height range.

[47] In Figures 11 and 12 the estimated meteor echo rate distributions as a function of time and height are shown as contour plots for 2002 and 2003 respectively. Figures 11a, 11c, 12a, and 12c show the number of echoes collected divided in 1-hour and 2-km bins for a whole month. Figures 11b, 11d, 12b, and 12d show the composite day version of Figures 11a, 11c, 12a, and 12c. Plots to the right of the contour plots show the

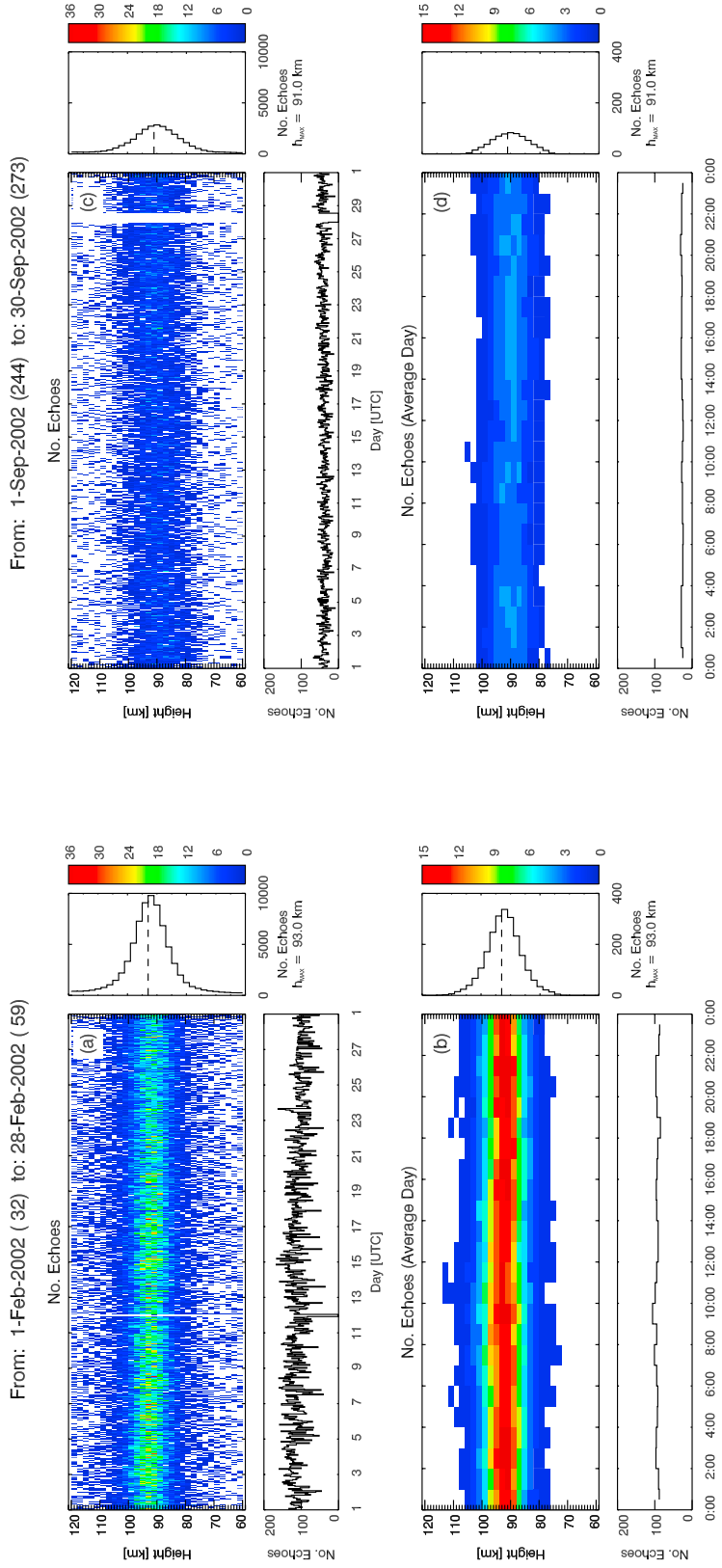


**Figure 11.** Height-time distributions of meteors for (a and b) a SH summer month (February) and (c and d) a SH winter month (September) in 2002. Figures 11a and 11c show the distributions for the whole month. Figures 11b and 11d show the distributions for an averaged day. Images are accompanied by their corresponding time and height histograms.

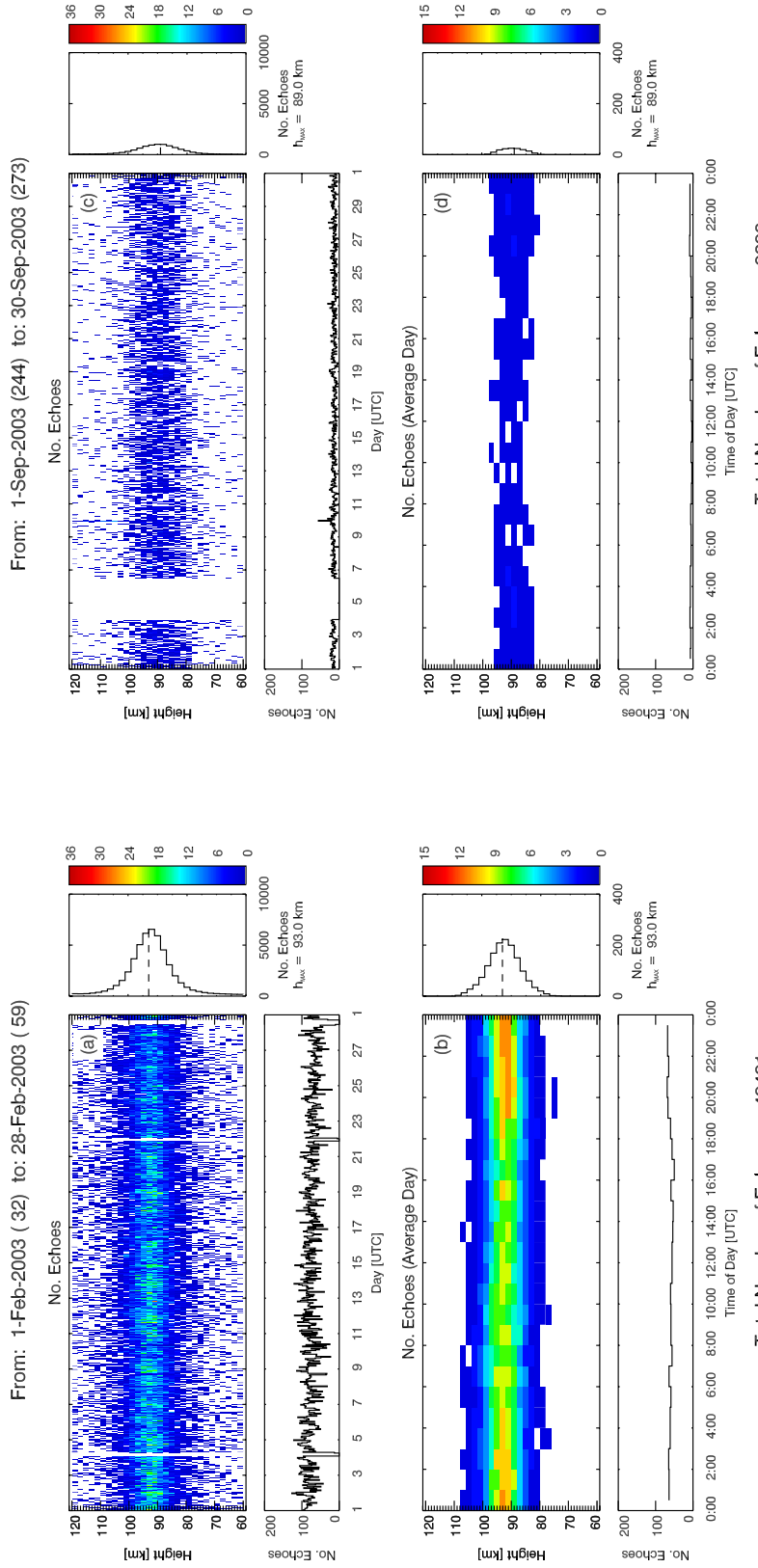


**Figure 12.** As in Figure 11 but for year 2003.

corresponding height distributions independent of time, while plots underneath the contour plots show the time distributions independent of height. The contour plots in Figures 11a, 11b, 12a, and 12b represent observations during a Southern Hemisphere (SH) summer month (February), while the contour plots in Figures 11c, 11d, 12c, and 12d represent observations at the end of the SH winter (September).

[48] It can be observed from the meteor height distributions (histograms to the right of Figures 11a–11d and 12a–12d) that the majority of meteor events are seen between 90 and 95 km. It also is observed that the height distributions are slightly higher ( $\sim 93$  km) during the SH summer than the SH winter ( $\sim 90$  km) in agreement with the usual cooling of the mesopause region during the summer. The cooling produces density enhancement at higher altitudes that leads meteoroids to ablate higher in the atmosphere.

[49] The composite day time distributions (plots beneath Figures 11b, 11d, 12b, and 12d) show no significant diurnal variability as it is observed at midlatitudes [e.g., *Valentic et al.*, 1996b; *Holdsworth et al.*, 2004a] or at lower polar latitudes [e.g., *Singer et al.*, 2004]. However, a strong seasonal variability is observed. The echo rates detected during the summer are about 3 times higher than during the winter months.

[50] Figures 13 and 14 show the AOA distributions of the postprocessed meteor echoes for 2002 and 2003, respectively. Again observed data during a SH summer month (Figures 13a–13d and 14a–14d) and a SH winter month (Figures 13e–13h and 14e–14h) are presented. The polar coordinates used to represent some of the results should be interpreted as follows: the distance from the center is the zenith angle (origin of the coordinate system represents vertical and concentric circles are spaced  $30^\circ$ ), the angle with respect to one of the baselines represents the azimuth or polar angle on the horizontal plane, and the color represents the plotted variable (echo rate or range to meteor). The plots for each month show the average number of echoes per day as a function of the AOA in Figures 13a, 13e, 14a, and 14e. The echoes were grouped in  $5^\circ$  elevation and  $10^\circ$  azimuth bins. Figures 13b, 13f, 14b, and 14f show the range of the collected meteor echoes as a function of the AOA. Every single meteor is represented as a pixel in Figures 13b, 13f, 14b, and 14f. This is done as a quality control check. As it is expected the echo range increases as the echoes are detected farther away from the local zenith. Figures 13c, 13g, 14c, and 14g show the composite day view of the meteor echo rate distributions as a function of elevation angle and time of day. Figures 13d, 13h, 14d, and 14h show the composite day view of the meteor echo rate distributions as a function of azimuth angle and time of day.

[51] The echo rate distributions shown in Figures 13 and 14 also reveal the same seasonal variation observed in the height-time distribution plots (Figures 11 and 12) with echo rates substantially higher during the summer than during the winter. The enhanced echo rate areas in the distributions as a function of AOA (Figures 13a, 13e, 14a, and 14e) show the regions in the sky where most of the power is transmitted ( $0^\circ$ ,  $90^\circ$ ,  $180^\circ$ , and  $270^\circ$  meridians and  $\sim 30^\circ$  elevation angle). The high concentration of echoes seen at  $\sim 30^\circ$  elevation angle is also observed in the distributions as a function of elevation angle and time of day (Figures 13c, 13g, 14c, and 14g); these distributions also show that there is no significant diurnal variability in these distributions. We fitted Gaussian curves to the elevation echo rate distributions at different times and found that the mean is  $\sim 26.5^\circ$ , the standard deviation is  $\sim 9^\circ$ , and the full width at half maximum (FWHM) is  $\sim 20^\circ$  (the width of the Gaussian distribution at the points where the amplitude is half the maximum). These values are influenced by the antenna patterns which are not isotropic, especially the yagi antennas used for transmission which have a theoretical FWHP beam width of  $40^\circ$  about an elevation angle of  $30^\circ$ . On the other hand, the distributions as a function of azimuth angle and time of day (Figures 13d, 13h, 14d, and 14h) do show a considerable variability in the echo rate with the time of day. All these features are persistent throughout the year even when the echo rates decrease significantly during the SH winter months. The fact that these distribution peaks appear roughly 6 hours apart for neighboring transmit antennas and follow the direction of the Earth rotation suggest the presence of a region in the sky where meteoroid activity is highly concentrated. This singular feature was first reported by *Janches et al.* [2004] who analyzed the diurnal and seasonal variability of the meteoric flux using data from the COBRA DAQ system. The majority of meteors are detected by the antenna that is pointing closest to the Earth's apex. Figure 15 shows the azimuth directions of enhanced echo rates at different times of the day for a SH summer and winter month inferred from the azimuth echo rate plots on Figures 13 and 14. We can observe that at different times of the day the meridians where most of the meteors are observed are in the direction the Earth is traveling around the sun. As it is expected, this means that as the Earth goes around the sun it sweeps more energetic meteoroids in the direction it is traveling because these meteoroids have the advantage of entering our atmosphere with the added speed of the Earth translation. However, this does not preclude the presence of space particles in any other direction, just their observability by radar. Our combined elevation and azimuth echo rate distributions suggest that most of the sporadic meteoroid activity detected at the South

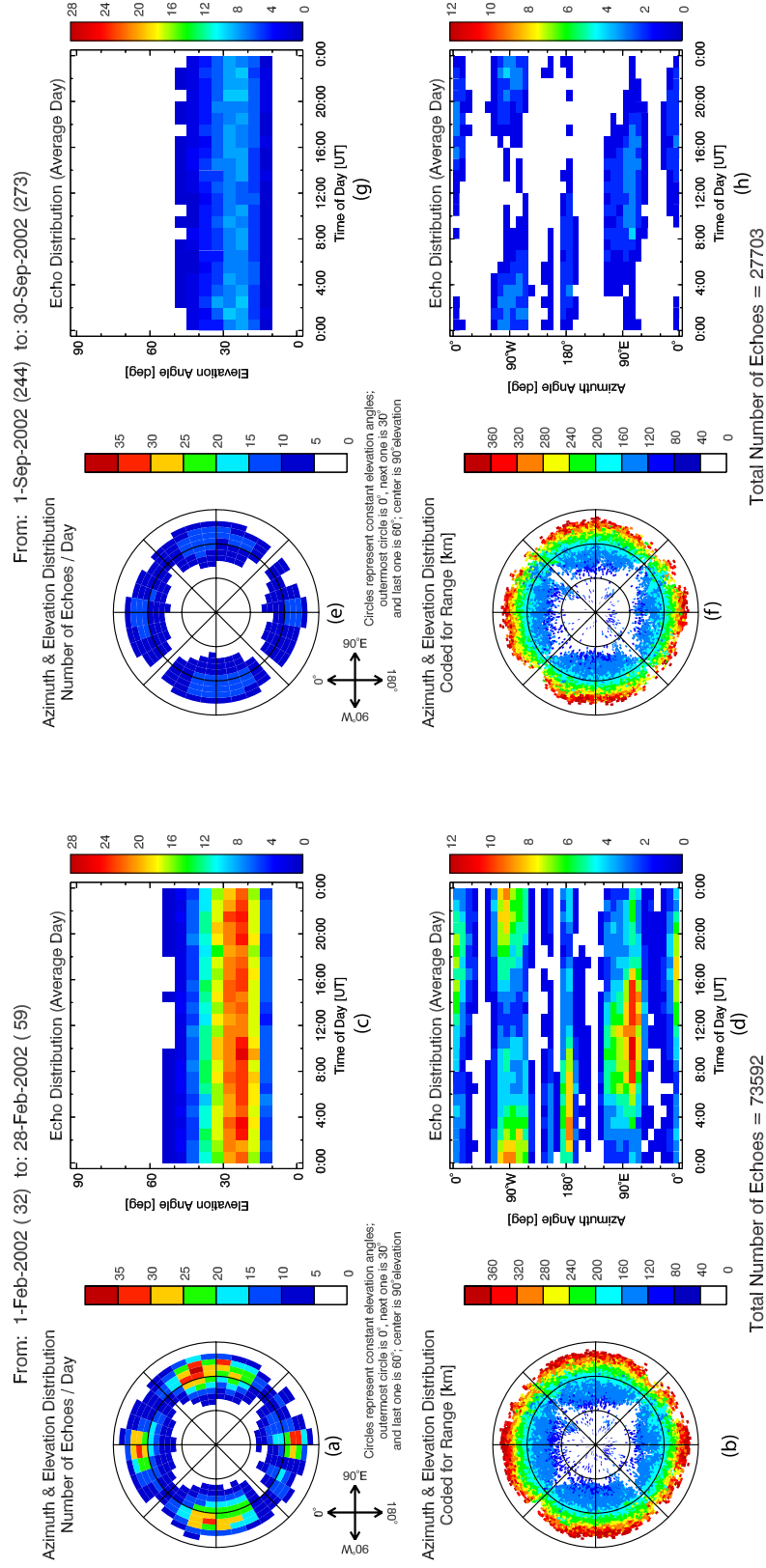


**Figure 13.** AOA distributions of meteors for (a–d) a SH summer month (February) and (e–h) a SH winter month (September) in 2002.

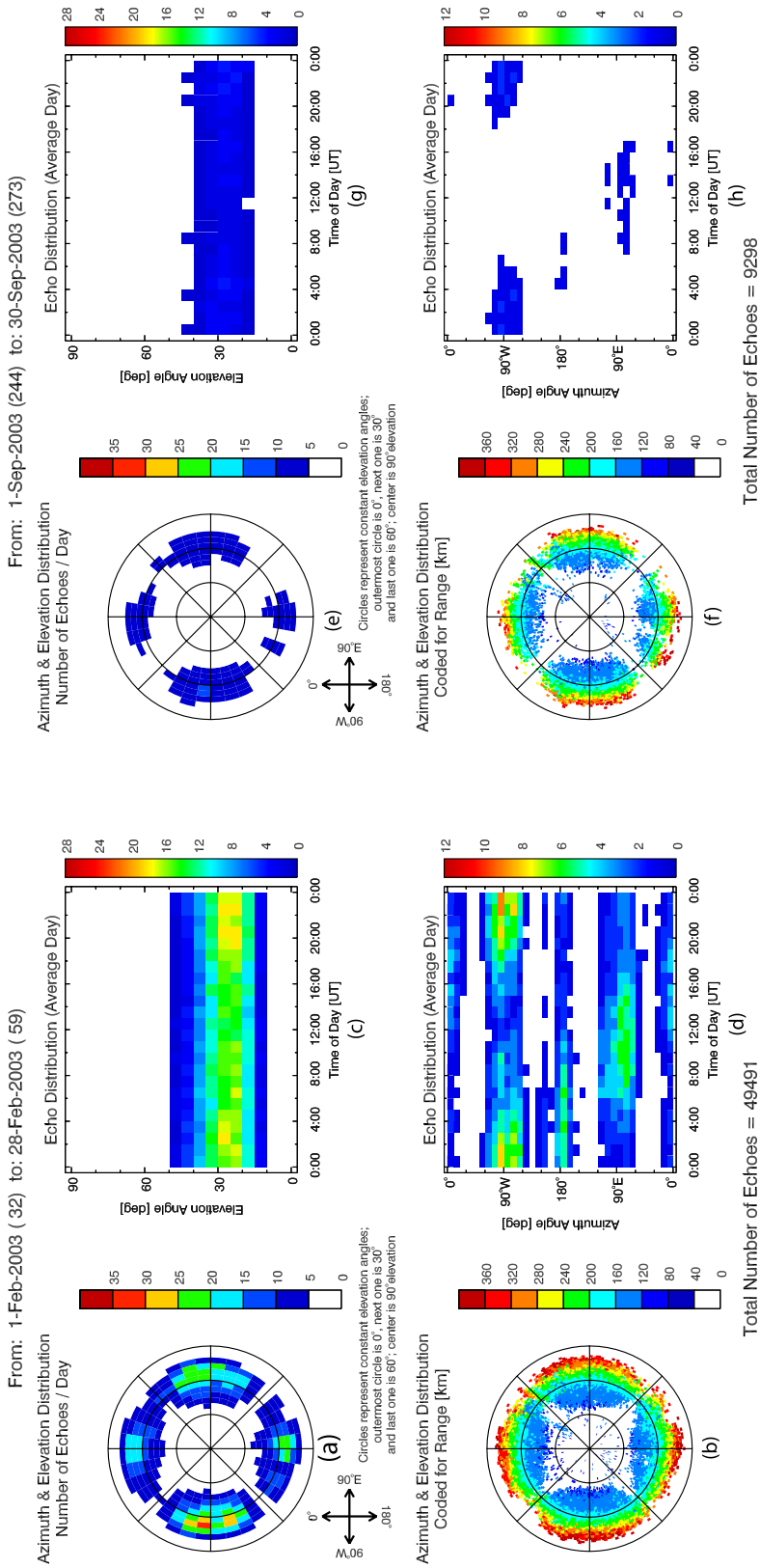


**Figure 14.** As in Figure 13 but for year 2003.

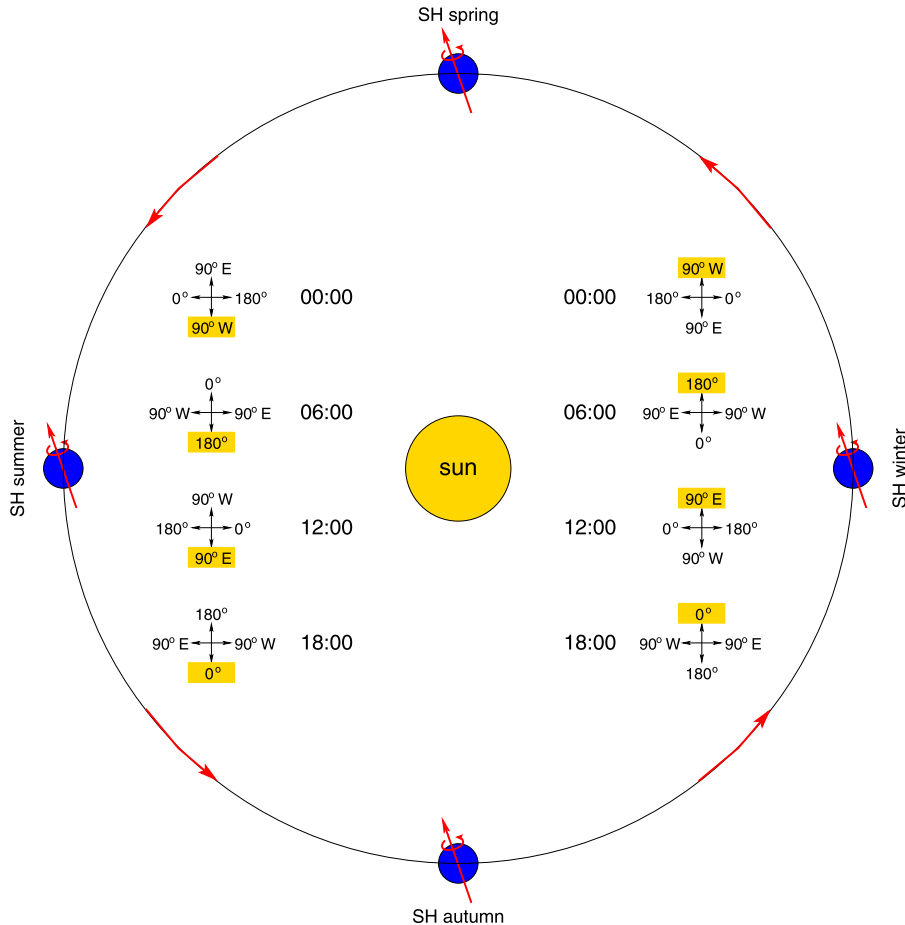


**Figure 15.** Directions of maximum echo rates in the azimuthal plane (highlighted meridian directions) as the Earth rotates around the sun for a SH summer and winter month. These directions were inferred from the azimuth echo rate information from Figures 13 and 14.

Pole is concentrated on the ecliptic plane, as previously argued by Janches *et al.* [2004].

## 7. Concluding Statements

[52] In this paper we described the South Pole VHF meteor radar. We also presented the postprocessing techniques that are implemented to extract information on the characteristics of the meteor flux. Several algorithms are implemented to perform the same task and a comparison of their performance is presented. In particular a new technique for AOA estimation is found to be more accurate than the widely used algorithm proposed by Jones *et al.* [1998].

[53] Analysis of the interferometric meteor data reveal a seasonal variability rather than a diurnal one with the peak of the activity observed during the SH summer. By contrast the peak of the meteor activity at

Arctic latitudes is observed during the Northern Hemisphere summer months [Singer *et al.*, 2004]. This asymmetry coupled with the elevation and azimuth meteor echo rate distributions presented in this paper suggest that the meteor activity is highly concentrated in a relatively small region of the sky around the ecliptic plane as previously pointed out by Janches *et al.* [2004]. The interferometric results presented in this paper point to a region with a FWHM around  $20^\circ$  in terms of elevation angle.

[54] A future goal is to increase the echo rate in order to get better statistics as well as expand our results horizontally and vertically. Under consideration are proposals to change the pointing direction of the yagi antennas and increase the peak output power of the system.

[55] Finally we are currently working on obtaining atmospheric wind and tide information measured with

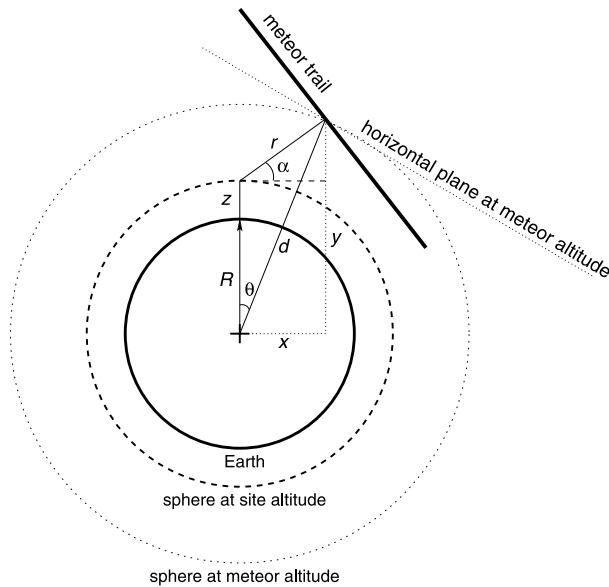


**Figure A1.** Geometry of meteor trail, Earth, and radar site.

the radar system and the results will be published in a future paper.

## Appendix A: Meteor Height Calculation

[56] We detail the method applied to calculate the meteor heights used, for instance, to plot the echo distributions in Figures 10, 11, and 12.

[57] In Figure A1 we define the following variables:

- $r$  range from radar to point of perpendicular reflection on meteor trail;
- $R$  radius of the Earth;
- $z$  radar site altitude above sea level;
- $\alpha$  elevation angle of the meteor;
- $\theta$  colatitude of meteor detection;
- $d$  distance from the center of the Earth to the point of perpendicular reflection;
- $x$  projection of segment of length  $d$  on a horizontal axis;
- $y$  projection of segment of length  $d$  on a vertical axis.

[58] We can relate the variables defined above through these equations:

$$\begin{cases} x = d \sin \theta = r \cos \alpha \\ y = d \cos \theta = R + z + r \sin \alpha. \end{cases} \quad (\text{A1})$$

[59] We can calculate  $x$  and  $y$  since  $r$ ,  $R$ , and  $z$  are known, and  $\alpha$  is calculated from interferometry. Therefore  $d$  is

$$d = \sqrt{x^2 + y^2}. \quad (\text{A2})$$

[60] We define  $h$  as the height of the meteor trail above the Earth (i.e., above sea level). Thus

$$h = d - R. \quad (\text{A3})$$

[61] Combining equations (A1), (A2), and (A3):

$$h = \sqrt{(r \cos \alpha)^2 + (R + z + r \sin \alpha)^2} - R. \quad (\text{A4})$$

[62] **Acknowledgments.** This work has been supported by NSF grants ATM-0000957 and ATM-0336946 to the University of Colorado. Diego Janches' work is supported under NSF grants ATM-0422043 to the University of Colorado and ATM-05311464 to Northwest Research Associates, Inc. The authors also appreciate the help of David Holdsworth in running some of our data through his calibration routine to produce one of the sets of phase offsets used in this paper.

## References

- Avery, S. K., A. C. Riddle, and B. B. Balsley (1983), The Poker Flat, Alaska, MST radar as a meteor radar, *Radio Sci.*, 18(6), 1021–1027.
- Avery, S. K., J. P. Avery, T. A. Valentic, S. E. Palo, M. J. Leary, and R. L. Obert (1990), A new meteor echo detection and collection system: Christmas Island mesospheric wind measurements, *Radio Sci.*, 25(4), 657–670.
- Baldwin, M., T. Hirooka, A. O'Neil, S. Yoden, A. J. Charlton, Y. Hio, W. A. Lahoz, and A. Mori (2003), Major stratospheric warming in the Southern Hemisphere in 2002: Dynamical aspects of the ozone hole split, *SPARC Newslett.*, 20, 24–26.
- Chang, J. L., and S. K. Avery (1997), Observations of the diurnal tide in the mesosphere and lower thermosphere over Christmas Island, *J. Geophys. Res.*, 102(D2), 1895–1908.
- De la Peña, S., S. K. Avery, J. P. Avery, E. Lau, and D. Janches (2005), Wind measurements of MLT region using the Platteville, CO MEDAC 50 MHz meteor radar, *J. Atmos. Sol. Terr. Phys.*, 67(13), 1211–1215.
- Dowdy, A. J., R. A. Vincent, D. J. Murphy, M. Tsutsumi, D. M. Riggan, and M. J. Jarvis (2004), The large-scale dynamics of the mesosphere–lower thermosphere during the Southern Hemisphere stratospheric warming of 2002, *Geophys. Res. Lett.*, 31, L14102, doi:10.1029/2004GL020282.
- Forbes, J. M., Y. I. Portnyagin, N. A. Makarov, S. E. Palo, E. G. Merzlyakov, and X. Zhang (1999), Dynamics of the lower

- thermosphere over South Pole from meteor radar wind measurements, *Earth Planets Space*, 51, 611–620.
- Hernandez, G. (2003), Climatology of the upper mesosphere temperature above South Pole (90°S): Mesospheric cooling during 2002, *Geophys. Res. Lett.*, 30(10), 1535, doi:10.1029/2003GL016887.
- Hernandez, G., R. W. Smith, G. J. Fraser, and W. L. Jones (1992), Large-scale waves in the upper-mesosphere at Antarctic high-latitudes, *Geophys. Res. Lett.*, 19(13), 1347–1350.
- Hernandez, G., G. J. Fraser, and R. W. Smith (1993), Mesospheric 12-hour oscillations near South Pole, Antarctica, *Geophys. Res. Lett.*, 20(17), 1787–1790.
- Hernandez, G., J. M. Forbes, R. W. Smith, Y. Portnyagin, J. F. Booth, and N. Makarov (1996), Simultaneous mesospheric wind measurements near South Pole by optical and meteor radar methods, *Geophys. Res. Lett.*, 23(10), 1079–1082.
- Holdsworth, D. A., I. M. Reid, and M. A. Cervera (2004a), Buckland Park all-sky interferometric meteor radar, *Radio Sci.*, 39, RS5009, doi:10.1029/2003RS003014.
- Holdsworth, D. A., M. Tsutsumi, I. M. Reid, T. Nakamura, and T. Tsuda (2004b), Interferometric meteor radar phase calibration using meteor echoes, *Radio Sci.*, 39, RS5012, doi:10.1029/2003RS003026.
- Janches, D., S. E. Palo, E. M. Lau, S. K. Avery, J. P. Avery, S. de la Peña, and N. A. Makarov (2004), Diurnal and seasonal variability of the meteoric flux at the South Pole measured with radars, *Geophys. Res. Lett.*, 31, L20807, doi:10.1029/2004GL021104.
- Jones, J., A. R. Webster, and W. K. Hocking (1998), An improved interferometer design for use with meteor radars, *Radio Sci.*, 33(1), 55–65.
- McKinley, D. W. R. (1961), *Meteor Science and Engineering*, McGraw-Hill, New York.
- Mitchell, N. J., D. Pancheva, H. R. Middleton, and M. E. Hagan (2002), Mean winds and tides in the Arctic mesosphere and lower thermosphere, *J. Geophys. Res.*, 107(A1), 1004, doi:10.1029/2001JA900127.
- Ozovich, I., D. J. McEwen, G. G. Sivjee, and R. L. Walterscheid (1997), Tidal oscillations of the Arctic upper mesosphere and lower thermosphere in winter, *J. Geophys. Res.*, 102(A3), 4511–4520.
- Palo, S. E., and S. K. Avery (1993), Mean winds and the semiannual oscillation in the mesosphere and lower thermosphere at Christmas Island, *J. Geophys. Res.*, 98(D11), 20,385–20,400.
- Palo, S. E., and S. K. Avery (1996), Observations of the quasi-two-day wave in the middle and lower atmosphere over Christmas Island, *J. Geophys. Res.*, 101(D8), 12,833–12,846.
- Palo, S. E., Y. I. Portnyagin, J. M. Forbes, N. A. Makarov, and E. G. Merzlyakov (1998), Transient eastward-propagating long-period waves observed over the South Pole, *Ann. Geophys.*, 16, 1486–1500.
- Portnyagin, Y. I., J. M. Forbes, and N. A. Makarov (1997), Unusual characteristics of lower thermosphere prevailing winds at South Pole, *Geophys. Res. Lett.*, 24(1), 81–84.
- Portnyagin, Y. I., J. M. Forbes, N. A. Makarov, E. G. Merzlyakov, and S. E. Palo (1998), The summertime 12-h wind oscillation with zonal wavenumber  $s = 1$  in the lower thermosphere over the South Pole, *Ann. Geophys.*, 16, 828–837.
- Singer, W., J. Weiß, and U. von Zahn (2004), Diurnal and annual variation of meteor rates at the Arctic Circle, *Atmos. Chem. Phys.*, 4, 1355–1363.
- Stoica, P., and R. L. Moses (1997), *Introduction to Spectral Analysis*, Prentice-Hall, Upper Saddle River, N. J.
- Strauch, R. G., R. A. Kropfli, W. B. Sweezy, and W. R. Moninger (1978), Improved Doppler velocity estimates by the poly-pulse-pair method, paper presented at 18th Conference on Radar Meteorology, Am. Meteorol. Soc., Atlanta, Ga.
- Tabei, M., and B. R. Musicus (1996), A simple estimator for frequency and decay rate, *IEEE Trans. Signal Process.*, 44(6), 1504–1511.
- Valentic, T. A., J. P. Avery, and S. K. Avery (1996a), MEDAC/SC: A third generation meteor echo detection and collection system, *IEEE Trans. Geosci. Remote Sens.*, 34(1), 15–21.
- Valentic, T. A., J. P. Avery, S. K. Avery, M. A. Cervera, W. G. Elford, R. A. Vincent, and I. M. Reid (1996b), A comparison of meteor radar systems at Buckland Park, *Radio Sci.*, 31(6), 1313–1330.
- Valentic, T. A., J. P. Avery, S. K. Avery, and R. A. Vincent (1997a), A comparison of winds measured by meteor radar systems and an MF radar at Buckland Park, *Radio Sci.*, 32(2), 867–874.
- Valentic, T. A., J. P. Avery, S. K. Avery, and R. C. Livingston (1997b), Self-survey calibration of meteor radar antenna array, *IEEE Trans. Geosci. Remote Sens.*, 35(3), 524–531.
- Wang, S. T., D. Tetenbaum, B. B. Balsley, R. L. Obert, S. K. Avery, and J. P. Avery (1988), A meteor echo detection and collection system for use on VHF radars, *Radio Sci.*, 23(1), 46–54.
- Younger, P. T., D. Pancheva, H. R. Middleton, and N. J. Mitchell (2002), The 8-hour tide in the Arctic mesosphere and lower thermosphere, *J. Geophys. Res.*, 107(A12), 1420, doi:10.1029/2001JA005086.
- 
- S. K. Avery, E. M. Lau, and R. Schafer, Cooperative Institute for Research in Environmental Sciences, University of Colorado, 216 UCB, Boulder, CO 80309, USA. (elias.lau@colorado.edu)
- J. P. Avery, Department of Electrical and Computer Engineering, University of Colorado, 425 UCB, Boulder, CO 80309, USA.
- D. Janches, CoRA Division, Northwest Research Associates, 3380 Mitchell Lane, Boulder, CO 80301, USA.
- N. A. Makarov, Institute for Experimental Meteorology, Scientific Production Association TYPHOON, Obninsk 249020, Russia.
- S. E. Palo, Department of Aerospace Engineering, University of Colorado, 429 UCB, Boulder, CO 80309, USA.